

## SPITZER OBSERVATIONS OF EXTENDED LYMAN- $\alpha$ CLOUDS IN THE SSA22 FIELD

T.M.A. WEBB<sup>1</sup>, T. YAMADA<sup>2</sup>, J.-S. HUANG<sup>3</sup>, M.L.N. ASHBY<sup>3</sup>, Y. MATSUDA<sup>4,5</sup>, E. EGAMI<sup>6</sup>, M. GONZALEZ<sup>1</sup>, AND T. HAYASHIMO<sup>7</sup>

*Draft version December 4, 2008*

### ABSTRACT

We present the results of a Spitzer IRAC and MIPS 24 $\mu$ m study of extended Lyman- $\alpha$  clouds (or Lyman- $\alpha$  Blobs, LABs) within the SSA22 filamentary structure at  $z = 3.09$ . We detect 6/26 LABs in all IRAC filters, four of which are also detected at 24 $\mu$ m, and find good correspondence with the 850 $\mu$ m measurements of Geach et al. (2005). An analysis of the rest-frame ultraviolet, optical, near- and mid-infrared colors reveals that these six systems exhibit signs of nuclear activity (AGN) and/or extreme star formation. Notably, they have properties that bridge galaxies dominated by star formation (Lyman-break galaxies; LBGs) and those with AGNs (LBGs classified as QSOs). The LAB systems not detected in all four IRAC bands, on the other hand, are, as a group, consistent with pure star forming systems, similar to the majority of the LBGs within the filament. These results indicate that the galaxies within LABs do not comprise a homogeneous population, though they are also consistent with scenarios in which the gas halos are ionized through a common mechanism such as galaxy-scale winds driven by the galaxies within them, or gravitational heating of the collapsing cloud itself.

*Subject headings:* galaxies: formation – galaxies: high-redshift – infrared: galaxies – galaxies: starburst – galaxies: active – (ISM:) dust, extinction

### 1. INTRODUCTION

Understanding the complex physics of galaxy formation is one of the key goals of astronomy today. Observations at high-redshift show that the young universe was strikingly different than it is locally and while many high-redshift galaxy populations have low-redshift analogues, significant evolution is seen in their global properties such as their clustering strength (Coil et al. 2004; Le Fèvre et al. 2005), the shape of their luminosity function (e.g. Cirasuolo et al. 2008) and their overall contribution to the integrated background light (e.g. Webb et al. 2003) and the stellar mass density of the universe (Rudnick et al. 2006). Individually, the galaxies themselves are generally more violent and dynamic objects than typical galaxies today. They are more gas-rich, show higher levels of star formation and nuclear activity (Chapman et al. 2005; Fine et al. 2006), experience increased rates of major mergers (Patton et al. 2002), and exhibit signs of energetic outflows (Shapley et al. 2003). The role that these processes play in building and shaping galaxies is still poorly understood, as is the link between different evolutionary phases and the importance of properties such as mass and the local environment in driving evolution.

Hierarchical structure formation models predict, and observations confirm, that the first objects to form in the early universe will be highly clustered (e.g. Kaiser 1984; Giavalisco et al. 1998). For this reason, many studies of galaxy evolution focus on single large structures at high-redshift which, in addition to isolating the most active sites of structure formation at early times, provides large samples of equidistant galaxies over a range in mass, luminosity and evolutionary stages. Such studies of high density environments have recently detected a new population of extended Lyman- $\alpha$  (Ly $\alpha$ ) emitting nebulae at high-redshift (Fynbo et al. 1999; Keel et al. 1999; Steidel et al. 2000; Francis et al. 2001; Palunas et al. 2004; Matsuda et al. 2004; Dey et al. 2005). The properties of these so-called Ly $\alpha$  Blobs (LABs) indicate they are energetic phases in the formation of galaxies: they have projected physical extents of tens to several hundreds of kpc, Ly $\alpha$  luminosities of  $\sim 10^{44}$  erg s<sup>-1</sup>, and the Ly $\alpha$  emission is often morphologically irregular and dynamically complex. They are prevalent in high-density regions which exhibit other signs of intense star formation and active galactic nuclei (AGN) activity, though the extent to which this is a selection effect has not been adequately explored through unbiased studies (c.f. Prescott et al. 2008).

The largest published sample of extended LABs to date is presented in Matsuda et al. (2004, hereafter M04), within the SSA22 structure at  $z \sim 3.09$ . Originally discovered as an over-density of Lyman-break Galaxies (LBGs) (Steidel et al. 1998), subsequent narrow-band imaging of the SSA22 field (Steidel et al. 2000) revealed two giant LABs within the concentration with sizes > 100 kpc. Narrow-band imaging over a larger area by M04 assembled a sample 35 LABs with sizes above a few tens of kpc and luminosities of  $10^{42-44}$  erg s<sup>-1</sup>. They are imbedded within a large (> 60 Mpc) structure, traced by the fainter and smaller Ly $\alpha$  Emitter (LAE) population (Hayashino et al. 2004; Matsuda et al. 2005) consisting

Electronic address: webb@physics.mcgill.ca

<sup>1</sup> McGill University Department of Physics, 3600 rue University, Montréal, QC, H2A 2T8

<sup>2</sup> Astronomical Institute, Graduate School of Science, Tohoku University, Aramaki, Aoba-ku, Sendai 980-8578, Japan

<sup>3</sup> Harvard-Smithsonian Center for Astrophysics, 60 Garden Street, Cambridge, MA 02138

<sup>4</sup> Department of Astronomy, Graduate School of Science, Kyoto University, Kyoto 606-8502, Japan

<sup>5</sup> Optical and Infrared Astronomy Division, National Astronomical Observatory of Japan, 2-21-1 Osawa, Mitaka, Tokyo 181-8588, Japan

<sup>6</sup> Department of Astronomy, University of Arizona, 933 N Cherry Avenue, Rm. N204, Tucson, AZ 85721-0065

<sup>7</sup> Research Center for Neutrino Science, Graduate School of Science, Tohoku University, Sendai 980-8578, Japan

of at least three dynamically distinct filaments. The two brightest two LABs are located at the filamentary intersection.

Clearly, the SSA22 structure is a concentration of evolutionary activity and the large number of LABs within it provides us with an opportunity to conduct a more systematic study these enigmatic systems than has been done before. The primary outstanding question concerns the mechanism responsible for their intense Ly $\alpha$  luminosities and super-galactic sizes. While an obvious explanation is photo-ionization by an embedded source, many LABs do not contain UV-bright galaxies of sufficient luminosity (M04). Neither are they powered by interactions between radio-jets and the ambient intergalactic medium as they are radio-quiet, unlike the similar Ly $\alpha$  halos surrounding high-redshift radio galaxies (Reuland et al. 2003). Alternative scenarios hold that these systems are powered by shock heating from galaxy-wide superwinds (Geach et al. 2005; Colbert et al. 2006), driven by intense starbursts or AGN (Keel et al. 1999), or through gravitational heating during the collapse of a large primordial cloud (e.g. Smith et al. 2007).

Although exceptional UV and radio sources are not in general found within LABs, recent observations have shown that many (but not necessarily all) LABs are associated with infrared luminous galaxies (Champan et al. 2001; Geach et al. 2005; Colbert et al. 2006; Beelen et al. 2008). The work of Champan et al. (2001) and Geach et al. (2005) detected 5 of the M04 LABs at 850 $\mu$ m ( $> 3\sigma$  significance). It is notable that the Submillimeter Array has failed to detect the most luminous of these, LAB01 ( $S_{850\mu m} = 17$  mJy; Steidel et al. 2000) indicating either extended submillimeter emission ( $> 4''$ ) or multiple submillimeter emitters confused within the beam (Matsuda et al. 2007), a point we will return to in §4.2. Work with the MIPS camera on board Spitzer has also revealed infrared-luminous counterparts to a number of LABs including the largest currently known (Dey et al. 2005; Colbert et al. 2006). These results all imply classifications of ultra-/hyper-luminous infrared galaxies (ULIRGs/HyLIRGs), with infrared luminosities of  $\sim 10^{12-13} L_{\odot}$ . The relationship between the infrared luminous systems and their respective LABs is unclear, but a weak correlation between the counterpart bolometric luminosity and the Ly $\alpha$  luminosity suggests that the size and luminosity of the LAB is controlled by global, galactic sized processes such as superwinds.

In this paper we present the first mid-infrared study of a large sample of LABs within the SSA22 filament with IRAC (Fazio et al. 2004) and MIPS (Rieke et al. 2004) on board the Spitzer Space Telescope (Werner et al. 2004). We use these observations, along with supplementary data from the literature, archives, and our own optical observations, to identify the galaxies which are associated with the LABs and to investigate their nature and relation to the clouds. At  $z = 3.09$  these data sample the rest-frame near- and mid-infrared (NIR/MIR), and are sensitive to stellar emission, thermally radiating hot dust, and polycyclic aromatic hydrocarbon features (PAHs). The broad shape of the spectral energy distribution (SED) in this region provides a useful diagnostic of the energy production mechanism within each galaxy that is complementary to the optical/UV and far-infrared observations.

The paper is organized as follows: §2 describes the observations and data analysis techniques of the mid-infrared, optical and archival X-ray data; in Section §3 we present the infrared counterparts to the LABs; and §4 contains a discussion of the constraints on the nature of the counterparts, comparisons to previous studies, and implications for our understanding of the LABs and their relation to galaxy formation.

## 2. OBSERVATIONS AND ANALYSIS

### 2.1. The IRAC and MIPS Observations

The Spitzer IRAC (3.6, 4.5, 5.8, and 8.0  $\mu$ m) and MIPS (24  $\mu$ m) data are part of two GTO programs, PID #64 and #30328 (PI: Giovanni Fazio). The former obtained single pointing data while the latter obtained images over most of the LAE filament. Although 70 and 160 $\mu$ m data were also obtained in program #64, in this paper we only discuss the 24  $\mu$ m data.

In program #64, a  $\sim 5' \times 5'$  area was imaged with IRAC (AORID #4397824) and MIPS (AORID #4397568) with integration times of 6400 sec/pixel and 1120 sec/pixel, respectively. In program #30328, an area of  $\sim 375$  arcmin<sup>2</sup> was imaged with IRAC (AORIDs #17599488, 17599744, 17600000, 17600256, 17600512) with integration times ranging from 3000 sec/pixel to 7500 sec/pixel, out of which an area of  $\sim 225$  arcmin<sup>2</sup> was covered by all four wavelengths to a uniform depth of 7500 sec/pixel. This same area of  $\sim 225$  arcmin<sup>2</sup> was also imaged with MIPS (AIRIDs #17600768, 17601024) with an integration time of 1200 sec/pixel.

The IRAC data were combined using MOPEX in tandem with the IRACproc package (Schuster et al. 2006) version 4.2.1. The pixels in the final mosaics were chosen to be  $0''.86$  on a side so that the area subtended by each pixel was exactly half that of the native IRAC pixels. The MIPS data were reduced and mosaicked with the MIPS Data Analysis Tool (DAT) as described in Gordon et al. (2005). The 24  $\mu$ m images were resampled and mosaicked with half of the original instrument pixel scale ( $1''.25$ ).

Figure 1 illustrates the varying IRAC and MIPS coverage of the field. Of the 35 LABs discovered by M04, 32 are covered by all four IRAC filters (not covered are LAB17, LAB10, LAB 28). Of these, six are confused or contaminated by nearby bright objects (LAB03, LAB04, LAB13, LAB21, LAB30, LAB32). This yields a working sample of 26 LABs, of which 20 lie within the 225 arcmin<sup>2</sup> covered by MIPS and by all 4 IRAC filters to a uniform depth, except in the region of the single deep pointing. Figure 1 also shows the location of the  $\sim 200$  LBGs from Steidel et al. (2003), which constitute a comparison sample throughout the paper.

Photometry on the IRAC and MIPS images was performed using 3.4'' and 6'' diameter apertures respectively, and aperture corrections were applied to correct to total fluxes. Uncertainties were determined through the variance in the sky background within an aperture area, measured within an 80'' box surrounding each object, and the variation in depth seen in Figure 1 is reflected in the uncertainty variation in Table 1. Table 1 lists the IRAC, MIPS flux measurements or upper-limits for the LABs with coverage at all four IRAC filters; we also include the SCUBA measurements of Champan et al.

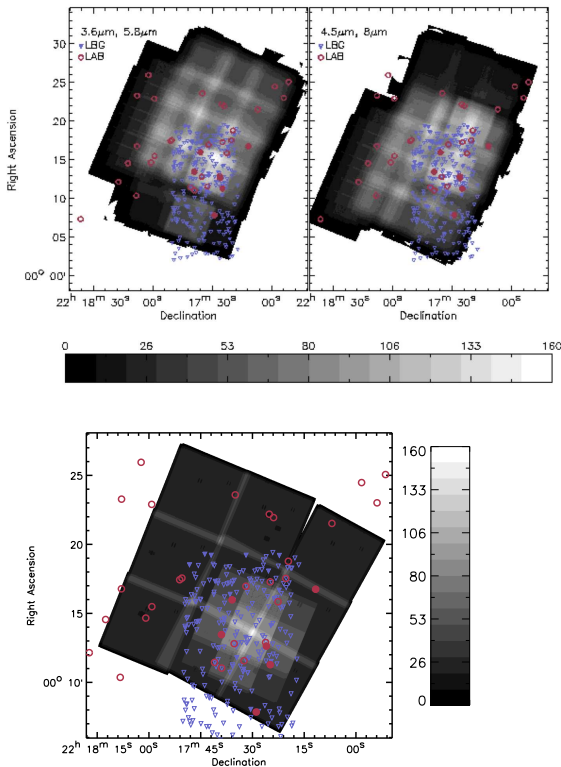


FIG. 1.— The Spitzer IRAC (top) and MIPS (bottom) coverage of the SSA22 field. The greyscale corresponds to the number of frames per pixel. Also shown are the locations of the LABs in the field (red circles) and the LBGs from Steidel et al. (2003) (blue triangles). In both cases the filled points denote objects detected at  $8.0\mu\text{m}$ .

(2001) and Geach et al. (2005) for reference.

## 2.2. MMT Optical Imaging

The SSA22 field was imaged at  $r'$  and  $i'$  (bands that approximate, but are not identical to, SDSS  $r$  and  $i$ ) during the nights of 2006 September 25, 26, and 27 with the Megacam camera McLeod et al. (2006) on the MMT atop Mt. Hopkins under conditions of stable sub-arcsecond seeing at a variety of position angles. The 500 s 36-chip exposures were reduced using standard methods and the custom IRAF reduction package Megared. Individual exposures were first bias-subtracted and trimmed before correcting bad pixels by nearest-neighbor interpolation and flattening with evening twilight flats. The coordinate system for each exposure was refined using the USNO B1 catalog and a priori knowledge of the relative orientations of the detector arrays; absolute accuracy in the positions of objects that are well-detected in single exposures should be better than  $0.2''$ .

Using photometry of stars common to the set of exposures, illumination corrections were computed to account for the contribution of OH skyglow to the twilight flats (B. McLeod, priv comm). These two corrections (one at  $r'$ , the other at  $i'$ ) were applied to all exposures in the appropriate bands. Sky templates were then created by median-filtering the object-masked science frames; these sky templates were used to fit and subtract large-scale gradients in the background of the individual exposures on a chip-by-chip basis. The utility SWarp was then used

to project all 36 chips from each exposure to a common coordinate grid with pixels  $0.32''$  on a side (four times the Megacam pixel size) and simultaneously to fit and remove large-scale ( $>82''$ ) structure from the backgrounds. Using coextensive SDSS photometry, the individual exposures were individually flux-calibrated and then correspondingly scaled/weighted when subsequently coadded to construct the final mosaics. The approximate  $5\text{-}\sigma$  depths of the final mosaics, after removal of artifacts, are roughly 27.1 and 25.9 AB mag at  $r'$  and  $i'$  respectively.

## 2.3. Archival X-ray Data

## 2.4. Chandra

The SSA22 field was observed with Chandra on 2001 July 10. After downloading from the archive, the data were reduced and analyzed using standard recipes with the CIAO package v3.3.0. The observation was performed continuously with no significant increase in background and a total livetime of 77.8 ks. The sources associated with the SSA22 LABs fall throughout the ACIS-S3 and ACIS-S2 chips. Exposure maps were computed for both chips and the resulting fluxes corrected accordingly.

## 2.5. XMM–Newton

XMM observations were taken on 2002 November 10 and 2002 December 15. After downloading from the archive, the data were reduced and analyzed using standard techniques and SAS v.7.0.0. Periods of high background were excluded from the data. During both observations, the EPIC MOS1/MOS2 and PN detectors were operated in full-window mode using the thin filter. In order to increase the signal to noise, we combined the individual MOS1+2 (i.e., one final MOS) and PN dataset for each observation. The total observing times were 256 ks and 110 ks for the MOS and PN detectors, respectively. Exposure maps were averaged and the resulting fluxes corrected accordingly.

## 2.6. X-ray Analysis

The Chandra and XMM datasets were searched for LAB counterparts using source detection algorithms such as *celldetect*, *wavedetect* and *ewavelet*. We detect two systems: LAB02 which has a previously published X-ray detection (Basu-Zych & Scharf 2004), is marginally detected by our analysis; and we detect, for the first time, LAB14. For the undetected LABs we calculated  $3\sigma$  upper limits on their fluxes derived using background levels close to the source positions. We have also clearly detected the two previously known QSO LBGs in the field from Steidel et al. (2003).

When available, Chandra and XMM provided similar flux limits; this is consistent with the different effective areas, exposure times, background and point-spread-function of each telescope and instrument. To compute the fluxes we have assumed a galactic absorption of  $N_H = 4.8 \times 10^{20} \text{ cm}^{-2}$  and an intrinsic photon energy power-law slope of  $\Gamma = 1$ .

## 3. RESULTS

### 3.1. Infrared Counterparts to LABs

We detect counterparts at  $> 5\sigma$  in all four IRAC filters for 6/26 LABs, where the term counterpart refers

TABLE 1  
INFRARED MEASUREMENTS OR LIMITS FOR THE COUNTERPARTS TO LABs

Name	RA	Dec	3.6 $\mu$ m ( $\mu$ Jy)	4.5 $\mu$ m ( $\mu$ Jy)	5.8 $\mu$ m ( $\mu$ Jy)	8.0 $\mu$ m ( $\mu$ Jy)	24 $\mu$ m ( $\mu$ Jy)	850 $\mu$ m (mJy) <sup>a</sup>
LAB01-a	22:17:26.0	00:12:36.6	7.3 $\pm$ 0.1	9.2 $\pm$ 0.2	11.5 $\pm$ 0.8	14.2 $\pm$ 1.0	51.3 $\pm$ 7.5	16.8 <sup>b</sup> $\pm$ 2.9
LAB01-b	22:17:26.1	00:12:32.5	8.4 $\pm$ 0.1	11.1 $\pm$ 0.2	14.7 $\pm$ 0.8	15.9 $\pm$ 1.0	57.5 $\pm$ 7.6	...
LAB02-a	22:17:39.3	00:13:22.0	5.6 $\pm$ 0.2	6.7 $\pm$ 0.2	8.3 $\pm$ 0.9	6.5 $\pm$ 1.4	< 45	< 3.6
LAB02-b	22:17:39.1	00:13:30.7	5.8 $\pm$ 0.2	7.8 $\pm$ 0.2	10.5 $\pm$ 0.9	15.4 $\pm$ 1.4	< 45	< 3.6
LAB05	22:17:11.7	00:16:44.3	7.7 $\pm$ 0.1	9.4 $\pm$ 0.2	10.1 $\pm$ 1.0	12.4 $\pm$ 1.3	< 40	5.2 $\pm$ 1.4
LAB14	22:17:35.9	00:14:58.8	7.4 $\pm$ 0.1	10.6 $\pm$ 0.2	15.0 $\pm$ 0.8	19.6 $\pm$ 1.1	71.3 $\pm$ 9.8	4.9 $\pm$ 1.3
LAB16	22:17:25.9	00:11:17.3	5.8 $\pm$ 0.1	7.3 $\pm$ 0.2	9.6 $\pm$ 1.0	15.2 $\pm$ 1.5	84.3 $\pm$ 9.6	< 16.0
LAB18-a	22:17:29.0	00:07:50.2	7.3 $\pm$ 0.2	8.7 $\pm$ 0.3	15.7 $\pm$ 1.5	19.2 $\pm$ 1.6	123.8 $\pm$ 10.6	11.0 $\pm$ 1.5
LAB18-b	22:17:29.0	00:07:43.2	4.9 $\pm$ 0.2	7.8 $\pm$ 0.3	8.6 $\pm$ 1.5	17.6 $\pm$ 1.6	< 55	...
LAB06	22:16:51.4	00:25:03.6	5.2 $\pm$ 0.3	5.4 $\pm$ 0.8	< 9.0	< 25.0	...	< 9.0
LAB07	22:17:41.0	00:11:26.1	2.8 $\pm$ 0.4	2.8 $\pm$ 0.3	< 7.0	< 10.0	< 53	< 8.0
LAB08	22:17:26.2	00:12:55.2	2.6 $\pm$ 0.1	1.0 $\pm$ 0.2	< 4.0	< 5.0	< 38	< 27
LAB09	22:17:51.2	00:17:28.0	2.3 $\pm$ 0.2	2.2 $\pm$ 0.2	< 5.0	< 10.5	< 56	< 27
LAB11	22:17:20.3	00:17:32.2	3.0 $\pm$ 0.2	2.6 $\pm$ 0.2	< 5.0	< 6.0	< 42	< 27
LAB12	22:17:31.7	00:16:57.5	2.6 $\pm$ 0.2	3.0 $\pm$ 0.2	4.8 $\pm$ 0.9	< 6.0	< 52	< 8.0
LAB15	22:18:08.4	00:10:22.5	1.7 $\pm$ 0.3	1.8 $\pm$ 0.3	< 12.0	< 8.0	...	...
LAB19	22:17:19.6	00:18:44.7	2.8 $\pm$ 0.1	2.4 $\pm$ 0.2	< 4.0	< 5.5	< 49	< 27
LAB20	22:17:35.4	00:12:47.6	1.3 $\pm$ 0.2	< 1.0	< 4.0	< 7.5	< 44	< 8.0
LAB22	22:17:35.0	00:23:34.4	< 3.0	< 2.0	< 6.0	< 8.0	< 52	...
LAB23	22:18:08.0	00:23:15.5	< 1.5	< 4.0	< 13.0	< 27	...	...
LAB24	22:18:00.9	00:14:40.0	< 0.8	< 1.0	< 5.0	< 7.0	< 62	...
LAB25	22:17:22.6	00:15:51.6	1.2 $\pm$ 0.1	2.4	< 4.0	< 8.0	< 46	< 27
LAB26	22:17:50.4	00:17:33.3	< 1.0	< 1.0	< 5.0	< 10.0	< 57	< 27
LAB29	22:16:53.9	00:23:00.9	3.6 $\pm$ 0.3	< 4.0	< 8.0	< 24.0	...	...
LAB31	22:17:39.0	00:11:02.4	1.1 $\pm$ 0.3	< 1.5	< 6.0	< 8.0	< 50	< 27
LAB33	22:18:12.0	00:14:32.6	1.8 $\pm$ 0.2	2.1 $\pm$ 0.3	< 10.0	< 10.0	...	< 8.0
LAB34	22:16:58.4	00:24:29.2	1.8 $\pm$ 0.2	< 2.0	< 6.5	< 13.5	...	...
LAB35	22:17:24.8	00:17:17.0	1.4 $\pm$ 0.2	1.4 $\pm$ 0.2	< 4.5	< 6.0	< 45	< 27

<sup>a</sup>From Geach et al. (2005) and Champan et al. (2001)

<sup>b</sup>Because of the large uncertainty in the submm position the submm counterpart may be physically associated with either or both of the 8 $\mu$ m sources, though here we list it only once.

to objects found within the extent of the Ly $\alpha$  emission. The 4-band detected LABs are: LAB01, LAB02, LAB05, LAB14, LAB16, and LAB18 (maintaining the M04 nomenclature). All six lie within the MIPS image and all but two (LAB02; LAB05) also show 24 $\mu$ m emission; there is a tentative 24 $\mu$ m detection of LAB02 but it is at  $< 5\sigma$  and appears spatially offset from the 8 $\mu$ m detection.

Figure 2 shows the  $r'$ , 3.6 $\mu$ m, 8.0 $\mu$ m, and 24 $\mu$ m images of the 6 LABs, overlaid with Ly $\alpha$  contours from the M04 survey. The LABs can be divided into two distinct groups: LABs with sizes  $> 100$  arcsec<sup>2</sup> which have more than one galaxy within the extent of the Ly $\alpha$  emission (LAB01, LAB02, LAB18); and the smaller,  $< 100$  arcsec<sup>2</sup> LABs which are coincident with only one possible counterpart (LAB05, LAB14, LAB16). Below we discuss the specifics of each source.

**LAB01:** With a projected physical size of 150 kpc, this is the largest LAB within the SSA22 filament and indeed is one of the largest discovered to date (see also Dey et al. (2005)). It has been the focus of a number of studies (Steidel et al. 2000; Champan et al. 2001; Bower et al. 2004; Geach et al. 2007). Here we briefly summarize the relevant points and refer the reader to the earlier work for details.

Multiple systems have been detected within the large extent of the Ly $\alpha$  emission including a strong submillimeter emitter ( $S_{850\mu\text{m}} \sim 17$  mJy) and a radio source at 1.4 GHz, (Champan et al. 2001)); these may be the same

object, though the uncertainty on the submillimeter position is substantial and is spatially consistent with other counterparts. Deep HST STIS imaging by Champan et al. (2001) reveals four faint optical components in the central region of LAB01 and we recover these structures, with much lower spatial resolution, in the  $r'$ -band MMT image (Figure 2). One of these (J2 in Champan et al.) is an Extremely Red Object and is a second possible counterpart to the submillimeter source, but is offset from the radio position.

Geach et al. (2007) investigated the mid-infrared properties (rest-frame NIR) of LAB01 (and LAB02) using a subset of the data presented here. For clarity we have adopted the counterpart labels of that paper in Figure 2, for LAB01 and LAB02. There are five objects detected at 3.6 $\mu$ m within the extent of the Ly $\alpha$  emission which Geach et al. have denoted **a,b,c,d, e**. Sources **e** and **d** are only detected at 3.6 $\mu$ m and 4.5 $\mu$ m and have blue colors ( $S_{3.6\mu\text{m}} > S_{4.5\mu\text{m}}$ ) consistent with  $z < 1$  galaxies. Source **c** is the LBG C11 (Steidel et al. 2000) which is a member of the filament and therefore possibly physically associated with the LAB, though as noted by Geach et al. and Bower et al. (2004) it appears kinematically distinct from the Ly $\alpha$  emission.

Sources **a** and **b** are detected in all four IRAC bands as well as MIPS 24 $\mu$ m. LAB01-a is located in the central region of the cloud, close to a peak in the Ly $\alpha$  emission, but its counterpart at shorter wavelengths remains unclear. For the remainder of the paper we have adopted

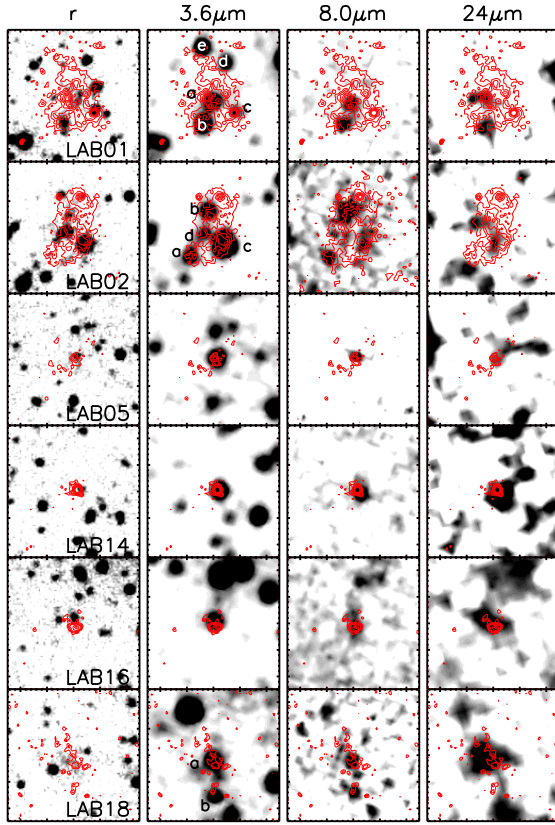


FIG. 2.— Postage stamps of the  $8\mu\text{m}$  detected LABs at  $r'$ ,  $3.6\mu\text{m}$ ,  $8.0\mu\text{m}$ , and  $24\mu\text{m}$  with the Lyman- $\alpha$  contours overlaid in red (Matsuda et al. 2004). North is up and east to the left. The distance between large tick marks corresponds to  $5''$ , and each image is  $25'' \times 25''$  in size.

the ERO mentioned above as it is the closest object to the  $3.6\mu\text{m}$  and  $24\mu\text{m}$  centroids and is optically red, though a second possibility is the radio source. We note however that the similar  $r'$ -band flux of the ERO and radio source means none of our key results are strongly dependent on this assumption.

LAB01-b has not received much attention thus far, perhaps because it lies in the outer region of the Ly $\alpha$  cloud and  $\sim 7''$  from the submillimeter centroid. The optical and near-infrared imaging reveals two objects separated by  $2''$ , one of which is substantially brighter than the other and coincident with the center of the  $3.6\mu\text{m}$  emission; hereafter we take this brighter system to be the IRAC source.

The IRAC-MIPS photometry of LAB01-a and -b are very similar: both are detected in all 4 IRAC filters and MIPS- $24\mu\text{m}$  at roughly the same flux levels. As discussed in §4, their infrared colors are indicative of  $z \sim 3$  galaxies and we here conclude that both systems are associated with the SSA22 filament and LAB01. As already noted by Geach et al., the projected separation is  $\sim 30$  kpc and hence this may be an interacting system within the LAB, though no clear evidence of this is seen in the deep optical imaging.

LAB01 has now been observed with a number of different submillimeter facilities. The original SCUBA de-

tection (Champan et al. 2001) is the strongest and most significant at  $S_{850\mu\text{m}} = 16.8 \pm 2.9$  mJy, but the large beam (FWHM  $\sim 15''$ ) of the JCMT at  $850\mu\text{m}$  makes the positional uncertainty significant, and it is possible that more than one source within the LAB is contributing to the submillimeter flux. Such a scenario would explain both the very high submillimeter emission measured by the JCMT and the recent non-detection of this LAB with the Submillimeter Array (SMA) (Matsuda et al. 2007). The SMA observations should have detected the source, unless it was extended beyond  $4''$  or composed of multiple fainter systems, confused within the JCMT beam, in which case the emission would be resolved by the SMA below the detection threshold. The  $24\mu\text{m}$  detections of both LAB01-a and -b mark them both as strong infrared emitters and thus possible submillimeter sources, and their separation of  $\sim 5$  arcsec is certainly well below the resolution limit of SCUBA at  $850\mu\text{m}$ .

This picture is confused however by two other data sets, which call into question the submillimeter measurements. The OVRO CO(4-3) observations (Chapman et al. 2004) detected a single object  $2''$  N of the ERO, which implies only a single submillimeter emitter, however the detection is only at a  $3.2\sigma$  significance and thus a second source of similar flux could lie just below the detection limit of these data. Recent observations taken with the AzTec submillimeter array on the Atacama Submillimeter Telescope Experiment at  $1\text{mm}$  (Kohno et al. 2008) however failed to detect any submillimeter emission, to a  $5\sigma$  limit of  $\sim 10$  mJy (Kohno et al. 2008). Given the large beam-size of  $\sim 38''$  at  $1\text{mm}$ , the existence of multiple submillimeter emitters cannot explain this non-detection.

**LAB02:** LAB02 is the second of three LABs in this sample with multiple objects within its large extent. Although this object has been identified as a possible submillimeter emitter, the  $850\mu\text{m}$  detection (Champan et al. 2001) is of significance ( $2.75\sigma$ ) and we consider this an unreliable detection. As first reported by Geach et al. (2007), and seen in Fig. 2, there are a number of systems detected in the IRAC imaging with very different observed optical and infrared colors. The brightest object in the group, object **c** in Geach et al., is a bright radio source and has  $S_{5.8\mu\text{m}}/S_{3.6\mu\text{m}} < 1$  and  $S_{8.0\mu\text{m}}/S_{4.6\mu\text{m}} < 1$ , consistent with a foreground galaxy at  $z < 1$ . Source **d** (not discussed in Geach et al.) is also consistent with a low redshift galaxy: it is detected in the optical through to  $4.5\mu\text{m}$ , with  $S_{4.5\mu\text{m}}/S_{3.6\mu\text{m}} < 1$ , but is not visible at  $5.8\mu\text{m}$  and  $8.0\mu\text{m}$ . The most likely physical counterparts to the LAB are therefore sources **a** and **b**. LAB02-a however is detected with a significance of only  $4\sigma$  at  $8.0\mu\text{m}$  and thus its color, while consistent with  $z \sim 3$ , is poorly constrained; for that reason although its photometry is listed in Table 1, it is considered an  $8\mu\text{m}$  non-detection for the remainder of the analysis.

Source LAB02-b lies in the outer region of the blob. It is not detected at  $24\mu\text{m}$  but has been associated with a Chandra X-ray source (Basu-Zych & Scharf 2004). Using archival data, we find a  $0.3\text{--}10$  keV flux level at its coordinates of  $(2.5 \pm 1.3) \times 10^{-15} \text{ erg s}^{-1} \text{ cm}^{-2}$  using the Chandra data and a power-law spectrum, consistent with the reported values of Basu-Zych & Scharf (2004). However, we find that it has a significance of  $\sim 2\sigma$  in these Chandra data (the source is not picked up as significant in our detection algorithms) and it is *not* detected in the



XMM datasets. Thus, we regard the X-ray detection as tentative: it is likely very faint and/or slightly extended so that the larger XMM PSF precludes a detection there. In the latter case, a deeper Chandra observations should clarify this issue.

**LAB05:** A single counterpart exists for this LAB. It is detected at all IRAC wavelengths, at  $r'$  and  $i'$ , at  $850\mu\text{m}$ , but not at  $24\mu\text{m}$ .

**LAB14:** LAB14 has only one possible counterpart and this is offset from the center of the LAB by  $\sim 1''$  in all bands. It is strongly detected at all wavelengths, from  $r'$  to  $850\mu\text{m}$ . The archival X-ray data have also revealed an X-ray source coincident with the IRAC position, heretofore unpublished. The object was detected with significances of  $\sim 2.5\sigma$  in *both* ACIS and MOS instruments (unfortunately it fell in between chip gaps in the PN instrument) and we thus consider it a very solid detection with a 0.3-10 keV flux level of  $2.1 \pm 0.8 \times 10^{-15} \text{ erg/s/cm}^2$

**LAB16:** A counterpart is detected in all four IRAC filters, as well as MIPS  $24\mu\text{m}$ . The peak  $\text{Ly}\alpha$  flux is offset from the  $r'$  and  $3.6\mu\text{m}/4.5\mu\text{m}$  counterpart by  $\sim 2''$ ; this may also be the case at the longer wavelengths,  $> 8.0\mu\text{m}$ , but the centroid poorly determined because of the lower S/N and the larger PSF.

**LAB18:** This LAB is detected at all infrared wavelengths, though is slightly confused by a foreground neighbor at  $24\mu\text{m}$ . LAB18 has no obvious single  $r'$ -band counterpart, but diffuse emission along the extent of the LAB is clearly visible. In Figure 2 we see two additional objects south of the main LAB emission which are detected at all four IRAC wavelengths, though not in the  $r'$  image, nor at  $24\mu\text{m}$ . The southern-most object is coincident with another  $\text{Ly}\alpha$  peak and has IRAC colors similar to the main LAB counterpart and consistent with a  $z \sim 3$  galaxy (see §4.1). The fainter, middle source however, shows no  $\text{Ly}\alpha$  flux and its color is contaminated by the main LAB counterpart, and we therefore have not included it as an LAB counterpart, although these three object may form a single interacting system. This LAB has a submillimeter detection of  $S_{850\mu\text{m}} = 11 \text{ mJy}$ , and with a separation of  $7''$ , both IRAC sources could contribute to the measured submillimeter flux, as may be the case with LAB01.

#### 4. DISCUSSION

##### 4.1. Observed Mid-Infrared Colors: Constraints on the Nature of the LAB Counterparts

At  $z \sim 3$  the IRAC filters sample the rest-frame NIR. In this region pure stellar populations are characterized by the stellar bump at  $1.6\mu\text{m}$ , with decreasing emission toward longer wavelengths. If cold dust is present within a galaxy, band emission from PAHs becomes important over the range of  $\sim 6 - 11 \mu\text{m}$  while warm dust produces emission that continues to rise as a power-law longward of  $1.6\mu\text{m}$  (e.g. Alonso-Herrero et al. 2006). These distinctly different SED shapes can, in principle, be exploited to diagnose the dominant power source of a galaxy (e.g. Lacy et al. 2004; Stern et al. 2005), but do suffer from important ambiguities and limitations, in particular beyond  $z \sim 2$ . In particular, red rest-frame NIR colors only indicate the presence of warm dust, and cannot discriminate between an AGN, with a nuclear warm dust component and an extreme infrared-luminous starburst whose warm dust is associated with HII re-

gions (e.g. Yun et al. 2008). Moreover, the separation of infrared-luminous galaxies into AGN and star-bursting systems is regardless an over-simplification, since the most luminous ULIRGs at low and high redshifts show evidence for both AGN activity and intense star formation and the optical/NIR emission will contain contributions from both processes. Nevertheless, an investigation of the rest-frame NIR-MIR SED shapes can provide basic clues to the nature of the galaxies residing within LABs.

In Figure 3 we show an IRAC color-color diagram for LAB counterparts detected in all four IRAC filters (e.g. Lacy et al. 2004). As discussed above, infrared power-law galaxies at low and high redshift inhabit a specific region of the diagram that is generally distinct from galaxies dominated by stellar emission in the optical/infrared, but which overlaps with the location of high-redshift star-forming ULIRGs. To illustrate this we plot the observed infrared colors of two representative SEDs with redshift, from  $z = 0$  to  $z = 3.09$ : the ULIRG Arp220 and a typical Irregular starburst galaxy from Coleman et al. (1980). Also shown are the observed infrared colors of  $8\mu\text{m}$ -bright LBGs within the SSA22 structure (Steidel et al. 2003) and the general  $8\mu\text{m}$ -selected population in the SSA22 field.

The LBGs exhibit rest-frame optical/NIR colors spanning almost an order of magnitude; while the bulk of the objects have colors consistent with a  $z \sim 3$  blue starburst galaxy, a number extend into the region of the diagram inhabited by ULIRGs and AGN. The LAB counterparts on the other hand are found without exception in the region of the redder LBGs and AGN/ULIRG templates and are not well described by a low-extinction starburst. In addition to the ULIRG/AGN ambiguity, it is also difficult to constrain the redshifts using the observed NIR colors: pure power-law systems in particular have a flat color-redshift relation. Nevertheless, one can see from Figure 3 that among the  $8\mu\text{m}$ -selected population power-law (and power-law-like) galaxies are rare ( $\sim 10\%$ ) and thus the likelihood that all five LABs have a randomly aligned unassociated power-law galaxy (and two in the case of LAB01) within the extent of the Lyman- $\alpha$  emission is remote ( $\lesssim 1\%$  assuming a generous alignment distance of  $5''$ ), and we therefore conclude that all seven systems have  $z = 3$  and are associated with their parent LAB.

Although the majority of the LABs were not detected in all four IRAC filters, nor MIPS  $24\mu\text{m}$ , we can still place constraints on their average properties through a stacking analysis of their infrared emission. For this exercise we take as the source position the coordinates of the  $3.6\mu\text{m}$  counterpart when available (the majority of the LABs) or if no counterpart exists at  $3.6\mu\text{m}$  we simply take the peak of the  $\text{Ly}\alpha$  emission; only 1 LAB is too extended to identify a clear peak/center and has no clear counterpart (LAB27), resulting in a sample of 20 systems, including LAB02-a. We detect stacked emission at  $> 5\sigma$  in all four IRAC filters and show the average color of the infrared-faint LAB systems in Figure 3. As we see, they are not simply lower luminosity versions of the  $8\mu\text{m}$  detected LABs, but rather are similar in color to the blue  $8\mu\text{m}$ -detected LBG population, implying they are more moderate starburst systems.

Returning to the infrared-bright LABs, the observed NIR colors require the presence of hot dust, heated by ei-

ther extreme dust-enshrouded star formation or feedback from a central AGN. As we now discuss however, the X-ray and MIR data indicate that AGN are present in some of these systems. First, turning to the X-ray results, two of the ten LBGs in this region are previously known optically confirmed QSOs (Steidel et al. 2003) which are strong X-ray emitters, and two of the seven LAB counterparts have weak X-ray emission (see §3). Here we use the Bauer et al. (2004) AGN/starburst classification scheme where a galaxy is considered an AGN if it satisfies any one of five X-ray or spectral conditions. Two of these conditions are  $L_X > 3 \times 10^{42}$  erg/s and  $f_{0.5-8.0\text{keV}}/f_R > 0.1$  which are satisfied by the two X-ray detected LABs ( $L_X \sim 4 \times 10^{43}$  erg/s and  $f_{0.5-8.0\text{keV}}/f_R \sim 1.5$ ). The individual and stacked X-ray limits for the remaining LABs are generous ( $L_X < 8 \times 10^{43}$  erg/s and  $L_X < 6 \times 10^{42}$  erg/s respectively) and are consistent with AGN according to these criteria. Deeper X-ray studies (Geach et al. 2008, in preparation) will clarify this issue.

In Figure 4 we look at the constraints placed by the  $24\mu\text{m}$  data through an investigation of the IRAC-MIPS colors. Here we are limited to the LAB and LBG comparison systems which are also detected at  $24\mu\text{m}$ . AGN-dominated systems generally inhabit the lower right of this diagram: hot dust enhances their observed  $8\mu\text{m}$  flux ( $2\mu\text{m}$  in the rest-frame) over the shorter wavelength stellar emission, but the lack of strong PAH features results in blue  $24\mu\text{m}-8\mu\text{m}$  colors, with some variation due to the steepness of the power-law. Star forming systems, on the other hand have less enhanced observed  $8\mu\text{m}$  (rest-frame  $2\mu$ ) emission, and thus blue  $8.0\mu\text{m}-4.5\mu\text{m}$  colors, but exhibit a wide variety of PAH strengths and therefore a range in  $24\mu\text{m}-8\mu\text{m}$  colors. Such a diagram has been used by other authors to attempt to identify the power sources within the very luminous SMG population (e.g Egami et al. 2004; Pope et al. 2006) which contain AGN and star-formation contributions, sometimes within the same objects, and, as seen in Figure 4, tend to populate the entire color space.

We see a clear separation of AGN and star-forming systems within the  $24\mu\text{m}$ -bright LBG population. It is interesting to see that the LAB counterparts occupy a small region of the color-space, and transition between these two populations. Thus while smoking-gun evidence of AGN in these systems is lacking, they appear distinct from the presumably pure star-forming LBG galaxies, but are also exhibit bluer NIR colors than AGN. We again perform a stacking analysis on the infrared faint LABs, this time restricting the sample to those which fall on the MIPS image. No MIPS flux is detected from these systems as a whole and we place an upper-limit on their observed  $24\mu\text{m}/8\mu\text{m}$  color on Figure 4. Here the separation between the infrared-bright and -faint LABs is less clear, though the infrared-faint LABs again lie blue-ward of the infrared-bright systems, toward the star-forming region of the diagram.

#### 4.2. Agreement with Submillimeter Results

Geach et al. (2005) observed 25 of the 35 LABs from Matsuda et al. (2004) at  $850\mu\text{m}$  and detected 5 at  $> 3\sigma$  significance. One of these, LAB10, lies outside of our imaged region. We find an almost one to one correspondence between the  $8\mu\text{m}$  and  $24\mu\text{m}$  detections presented here and the submillimeter detections. We recover all 4

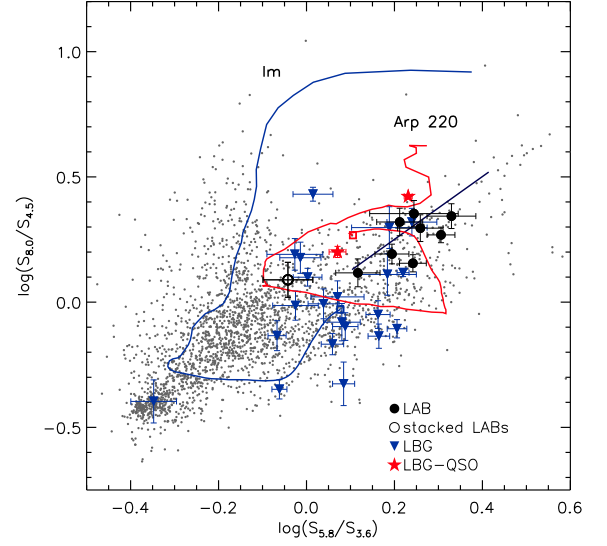


FIG. 3.— The IRAC color-color diagram. The grey points correspond to the entire  $8\mu\text{m}$ -selected catalog in the extended SSA22 field ( $>10\sigma$  in all 4 IRAC filters) and the filled black circles are those associated with the LAB counterparts ( $>5\sigma$  in all 4 IRAC filters). Overlaid are two template SED tracks with redshift: red denotes Arp220 and blue shows an irregular (Im) galaxy (Coleman et al. 1980). Tracks run from  $z = 0$  to  $z = 3.09$  with the higher redshift end denoted by an open square. Also shown (black line) is the location of pure power-law galaxies ( $S \propto \nu^\alpha$ ) with  $\alpha = [-0.5, -2.0]$ . LBGs in the SSA22 field with  $8\mu\text{m}$  detections are shown by the blue triangles; the two red stars are those LBGs confirmed as QSOs (Steidel et al. 2003). The stacked detection of the LABs which are not individually detected at  $8\mu\text{m}$  is shown by the open black circle.

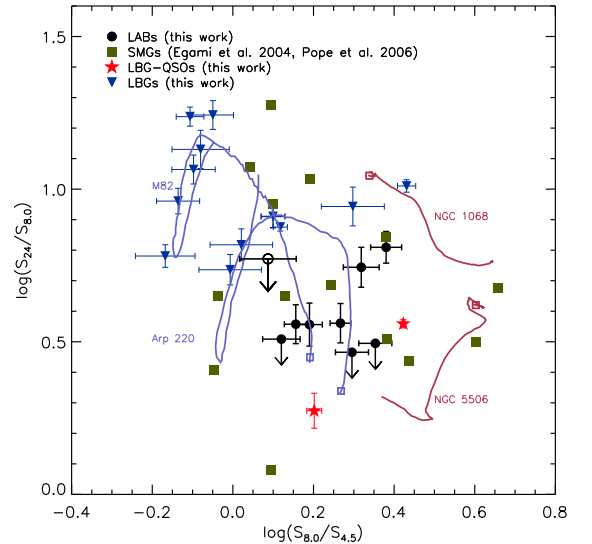


FIG. 4.— An IRAC/MIPS color-color diagram, restricted to those objects detected in all four IRAC filters, as well as at  $24\mu\text{m}$ . Filled black circles correspond to the LAB counterparts; filled blue triangles denote the LBGs; filled red stars show the LBGs which are confirmed QSO; and the solid green squares show SMGs with IRAC/MIPS detections which lie at  $z \sim 3$  from Egami et al. (2004) and Pope et al. (2006). Also shown is the stacked detection of the infrared-faint LAB (open black circle). Overlaid, to show the approximate distinction between the colors of AGN and ULIRGs are the template SEDs M82, Arp 220 (star-forming galaxies) and NGC 5506, NGC 1068 (dusty AGN).

of the  $850\mu\text{m}$  sources (for which we have data) at  $8\mu\text{m}$ . At  $24\mu\text{m}$  we fail to detect only LAB05 (limits are given in Table 1).

The  $24\mu\text{m}$ - $850\mu\text{m}$  flux ratios or limits are in good agreement with those measured for  $z \sim 3$  SMGs ( $< 0.02$ ) by Pope et al. (2006). As extensively discussed by Pope et al. (2006) such low values are consistent with galaxies such as Arp220 and Mrk273, which are not typical ULIRGs, and indicate higher levels of extinction and/or cooler dust temperatures than generally seen for ULIRGs. Cooler dust temperatures may be reached if the dust is spatially extended compared to local compact ULIRGs. This explanation is particularly interesting for LAB01: recent observations with the SMA (Matsuda et al. 2007) have failed to detect the  $S_{850\mu\text{m}} \sim 17\mu\text{Jy}$  source in the blob and this places a lower limit on its spatial extent of  $> 4''$  in the submillimeter (assuming it is signal dust enshrouded system). Such an explanation however cannot account for the failure of recent ASTE-AzTec observations to detect this source with a  $5\sigma$  limit of  $\sim 10\text{mJy}$  (Kohno et al. 2008).

As we showed in the previous section the  $8\mu\text{m}$  flux of the  $8\mu\text{m}$ -detected systems cannot be due only to stellar emission, but must be enhanced by the presence of hot dust, associated with prodigious star formation or due to a central dust enshrouded AGN. We have not detected any  $8\mu\text{m}$  source within an LAB which is not also detected at  $850\mu\text{m}$ , with the exception of LAB16, whose  $850\mu\text{m}$  limit is  $4\times$  higher than the 4 other  $850\mu\text{m}$  sources.

Adopting the average  $850\mu\text{m}$ - $8\mu\text{m}$  color for the infrared-bright LABs, a non-detection at  $850\mu\text{m}$  of  $< 3\text{mJy}$  (the approximate depth of Geach et al.) would lie below our  $8\mu\text{m}$  detection limit and therefore, based on this color alone, the infrared-faint LABs could simply be lower luminosity versions of the same kinds of systems. A non-detection at  $850\mu\text{m}$  (Geach et al. 2005) and  $24\mu\text{m}$  (this work) does not place very stringent limits on the bolometric luminosities of these systems however, and they remain compatible with ULIRG-level luminosities. Alternatively, the infrared-faint systems could be starburst galaxies with low extinction levels and correspondingly lower  $850\mu\text{m}$ - $8\mu\text{m}$  ratios. This scenario is in agreement with the stacked measurement on Figure 3 and with the additional color results discussed in the following sections. We can rule out with certainty however, dust enshrouded QSOs of similar rest-frame  $2\mu\text{m}$  luminosities, but which lack an extended cold dust component.

#### 4.3. The rest-frame UV-Optical-NIR properties

The bulk of the LAB sample is not detected longward of  $4.5\mu\text{m}$ , and in addition to the stacking analysis of the previous sections we can also look to the combination of  $3.6\mu\text{m}$  and/or  $4.5\mu\text{m}$  data with the NIR and optical imaging. In Figure 5 we show a rest-frame UV/optical/NIR color-color diagram for the LBGs and LABs. Here again, we see a clear separation between  $8\mu\text{m}$ -detected and non-detected systems, be they LABs or LBGs. The infrared-bright galaxies continue to show red colors into the rest-frame UV, indicating either older stellar populations and/or high levels of extinction. Notably, as seen in Fig 3 the infrared-faint LABs are well-separated in color from the infrared-bright systems, and are very similar to the general infrared-faint LBGs. The

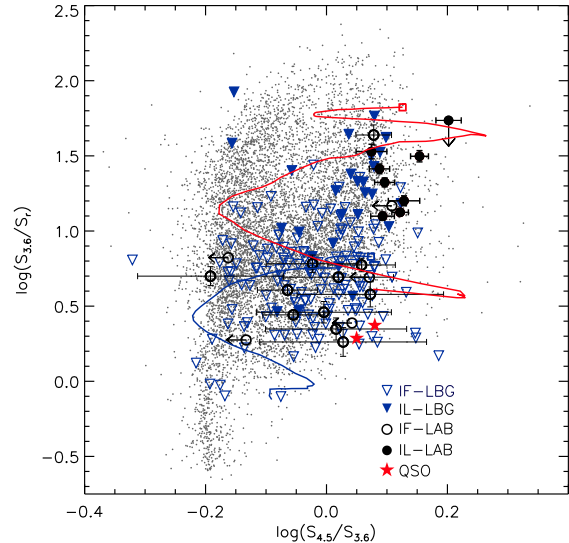


FIG. 5.— A rest-frame optical/UV color-color diagram. The small grey points correspond to the  $3.6\mu\text{m}$ -selected population in the SSA22 field. Points are as defined in 3 and 6 with the exception of the open triangles (individual  $8\mu\text{m}$ -faint LBGs) and the open circles (individual  $8\mu\text{m}$ -faint LABs). Here we denote  $8\mu\text{m}$ -detected LABs and LBGs as infrared-luminous (IL) and  $8\mu\text{m}$  non-detections as infrared-faint (IF). Also shown are the SED tracks (from  $z = 0 - 3.09$ ) for Arp 220 (red) and an irregular galaxy (Coleman et al. 1980) with the open square denoting  $z = 3.09$ .

exceptions are the two infrared-bright LBG-QSOs, which show extremely blue UV/optical colors.

In Figure 6 we show the observed  $8.0\mu\text{m}/3.6\mu\text{m}$  flux ratio as a function of observed  $8.0\mu\text{m}$  and, alternately,  $3.6\mu\text{m}$  flux. Again we compare to the LBG population, and add to the analysis the SMGs and QSOs as in Figure 4. In Figure 6(a) we see a correlation between the rest-frame  $2.0\mu\text{m}$  and the rest-frame NIR/optical colors, in the sense that galaxies which are more luminous at  $2.0\mu\text{m}$  exhibit redder colors, and the stacking analysis confirms that this relation continues to fainter levels. Visually, the slope of the relation appears to lie between a flat color-luminosity relation and that of the line representing constant  $3.6\mu\text{m}$  flux; that is, the relation results from an overall increase in luminosity and a enhancement of the  $2.0\mu\text{m}$  flux over the rest-frame optical. The rest-frame  $\sim 2.0\mu\text{m}$  is often taken as a proxy for stellar mass, however we have already argued that this wavelength is contaminated by AGN or intense star-formation in many of these systems. Indeed, the most luminous systems at observed  $8.0\mu\text{m}$  are the confirmed QSOs, followed by the LABs and then the infrared-bright LBG population. Though clearly not a complete comparison sample this does again hint that the LABs are transition objects between pure AGN and star-formation dominated systems.

In Figure 6(b) we plot the same color, but now against observed  $3.6\mu\text{m}$  flux. In addition to illustrating the spread in  $3.6\mu\text{m}$  luminosities, this allows us to probe the observed  $8\mu\text{m}$  flux of the comparison LBG population as a function of  $3.6\mu\text{m}$  flux. The statistical detection of the  $8\mu\text{m}$ -faint LABs fits within the general behavior of the LBGs, which become markedly bluer in the optical/NIR with decreasing  $3.6\mu\text{m}$  luminosity. Thus, the fainter, presumably less massive systems contain lower levels of dust, star formation and AGN activity.



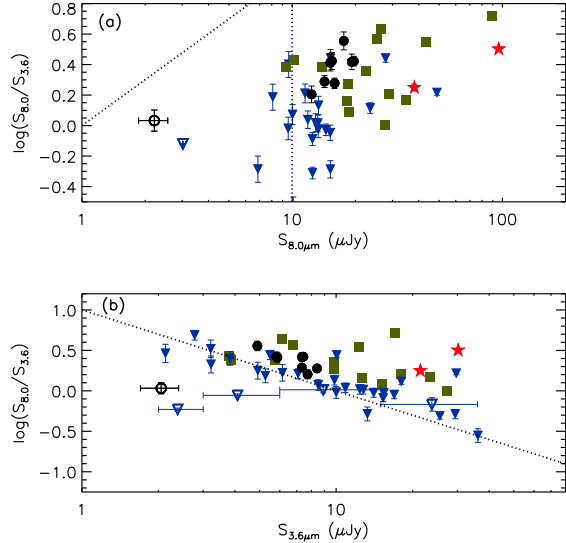


FIG. 6.— (a) The optical/NIR color as a function of rest-frame  $\sim 2\mu\text{m}$ . The vertical dotted line denotes the approximate  $5\sigma$  limit of the  $8\mu\text{m}$  data. The diagonal dotted line corresponds to the  $8\mu\text{m}/3.6\mu\text{m}$  flux ratio, at the  $3.6\mu\text{m}$  detection limit. Points are the same as in Figure 4. The filled black circles are the  $8\mu\text{m}$ -detected LAB counterparts; the filled blue triangles are the  $8\mu\text{m}$ -detected LBGs, with the two solid red stars corresponding to the confirmed QSOs, and the solid green squares are SMGs (Egami et al. 2004; Pope et al. 2006) for comparison. The open black circle and blue triangle below the  $8\mu\text{m}$  detection limit correspond to stacked measurements for the  $8\mu\text{m}$ -faint LABs and LBGs respectively. (b) The optical/NIR color as a function of rest-frame  $\sim 0.9\mu\text{m}$ . The dotted line shows the color limit at the  $8\mu\text{m}$  depth. The points are as in (a), however the LBG stacked detections include both  $8\mu\text{m}$ -faint and  $8\mu\text{m}$ -bright objects.

#### 4.4. $\text{Ly}\alpha$ excitation mechanisms and implications for galaxy evolution within the SSA22 structure

The two central questions concerning LABs are: what drives the extended  $\text{Ly}\alpha$  emission and, more generally, how are these structures related to galaxy formation? There are two basic scenarios for the relationship between the LABs and their counterpart galaxies. In the first, the embedded object is the excitation power source through processes such as photoionization by a strong UV emitter or by shock-heating due to super-galactic scale winds from a very strong starburst or a central AGN. In the second scenario, the  $\text{Ly}\alpha$  emission could be due to heating through gravitational collapse; in such a picture, the LAB and counterpart have no causal relationship (that is, the galaxy is not driving the  $\text{Ly}\alpha$  emission), but rather both mark sites of galaxy formation activity. In either case we might expect a correlation between the properties of the counterpart and the  $\text{Ly}\alpha$  halo; in the first case the correlation is obvious and causal while in the second case we might, for example, expect the most massive and luminous LABs to trace regions of correspondingly massive galaxy formation activity such as major-mergers, AGN, and extreme infrared starbursts.

Much work has been done to attempt to separate these different scenarios, but no common picture which works for all LABs has yet emerged. M04 extensively discussed the possible excitation mechanisms of the 35 LABs in SSA22. Using simple assumptions, such as a Salpeter IMF and an unhindered line of sight, they showed that  $\sim 1/3$  of the LABs do not contain galaxies which are

sufficiently UV-luminous to power the LABs. Of the six  $8\mu\text{m}$ -detected LABs discussed here, four (LAB01, LAB02, LAB05, LAB14) are not sufficiently bright in the rest-frame UV unless the bulk of the ionizing radiation is emitted away from our line of sight. This is not an unreasonable explanation since all six objects are dusty and IR-luminous, as evidenced by their  $8\mu\text{m}$ ,  $24\mu\text{m}$ , and/or  $850\mu\text{m}$  emission. The remaining LABs however, have UV/optical/IR colors which imply lower levels of dust extinction and are therefore unlikely to be highly obscured, but still lack obvious UV emitters.

By probing both hot and cold dust emission a number of authors (Geach et al. 2005; Colbert et al. 2006; Dey et al. 2005) have shown that a small fraction of LABs host infrared-bright systems of ULIRG and HyLIRG luminosity levels and importantly, that the inferred bolometric luminosity of these systems is weakly correlated with the  $\text{Ly}\alpha$  luminosity, though roughly three orders of magnitude larger. To the infrared-bright sample of Geach et al. (2005) we add LAB16; although not detected at  $850\mu\text{m}$  we may extrapolate from the  $24\mu\text{m}$  flux (assuming a similar SED as the other infrared-bright LABs) and find that LAB16 follows the roughly same  $L_{\text{Ly}\alpha}$ - $L_{\text{bol}}$  relation. As argued by Geach et al. (2005), this suggests that the process which heats the dust, i.e. a powerful AGN or intense star formation, is also responsible for exciting the gas halo, and a natural mechanism for this is galaxy-scale winds; however, this relation could simply indicate a natural non-causal correlation between the size of the collapsing gas cloud and the galaxy formation activity occurring within it.

We can use the data presented here to add to these studies by directly probing the nature of the LAB counterparts, though as with the earlier work this cannot prove a causal connection between the embedded galaxy and the gas emission. Throughout the paper however we have included similar analyses on the LBG population within the SSA22 structure, with the motivation that a comparative study of those systems which do not exhibit extended  $\text{Ly}\alpha$  emission might further elucidate the processes responsible for the LABs.

We can divide the sample into two distinct groups: those systems, be they LBGs or LABs, which are detected at  $8\mu\text{m}$ , hereafter referred to as infrared-luminous (IL), and galaxies which are not detected at  $8\mu\text{m}$ , or infrared-faint (IF). Let us first discuss the IL sample. The MIR/NIR colors of the LBGs and LABs within this group are similar and are best described by either a dusty AGN power-law or an intense starburst ULIRG. Some of these have been detected in the X-ray with emission levels consistent with though not uniquely indicative of AGN. Differences begin to arise when we look at the UV/optical colors or include the rest-frame  $6\mu\text{m}$  in the analysis (Figures 5 and 4). The bulk of the LBG population is systematically bluer in UV/optical color than the LABs, while in MIR color there is a clear continuum of colors between the bulk of the LBGs, the LABs and the LBG-QSOs. Finally, in Figure 6 we see hints of a similar gradient in rest-frame  $2\mu\text{m}$  luminosity, such that the LABs lie between the confirmed LBG-QSO and the remainder of the LBG population. This hints that, like the SMG population, IL-LABs may harbor deeply enshrouded AGN, in addition to intense star formation.

The following toy-model might therefore be proposed

for these systems. The most luminous LABs are powered through galaxy-scale superwinds driven by intense star formation and AGN activity. As the AGN grows it eventually becomes powerful enough to completely blow-out the gas cloud and enshrouding dust and emerges as a naked AGN, still luminous at the shorter IR wavelengths but no longer an LAB. It is not clear from these data how the IL-LBGs fit into this picture. As suggested by Dey et al. (2005), one might speculate that the brightest LBGs are older systems whose AGN has turned off, hence their lower  $8\mu\text{m}$  fluxes, but whether a LAB phase is common to all LBGs is not yet clear. This scenario could however account for the variety of morphologies of the LABs and the location of the galaxies within them. Take for example the three largest LABs, LAB01, LAB02 and the LAB of Dey et al. (2005): all have likely AGN counterparts near the edge of the  $\text{Ly}\alpha$  emission, and these may be systems caught in the process of emerging from their parent cloud.

One might posit that an AGN is required to power the intense  $\text{Ly}\alpha$  emission, and this is the root of the difference between the LBG without extended  $\text{Ly}\alpha$  emission and LAB populations. This seems at odds however, with the IF systems. Though the data are sparse for these groups, we see no difference between the properties of the IF LAB counterparts and the IF LBGs: both appear to be pure star-forming systems with roughly similar masses (now using the  $8\mu\text{m}$  luminosity as a proxy for mass). In these systems AGN are not driving the  $\text{Ly}\alpha$  emission, nor can the presence of a  $\text{Ly}\alpha$  halo for one group but not the other be explained by obvious differences in their counterpart properties.

It seems more likely therefore that the difference is in evolutionary phase over a cross-section of masses; those galaxies with extended  $\text{Ly}\alpha$  emission are in earlier phases of formation than the older LBGs. In this case the  $\text{Ly}\alpha$  emission could be powered by superwinds, as discussed above, or may be unrelated to (but still correlated with) the embedded galaxies and driven instead by gravitational heating, as suggested, for example, by Dey et al.

(2005) and Smith et al. (2007). Again, however, such a scenario would seem to imply that an LAB phase is common to all systems, unless secondary factors such as morphology play a role.

#### 4.5. Conclusions

We have used mid-infrared imaging from Spitzer IRAC and MIPS  $24\mu\text{m}$  to investigate the nature of a large sample of LAB systems within the SSA22 filament at  $z = 3.09$ . We have detected 6/26 of the objects in all four IRAC filters, with four also detected with MIPS  $24\mu\text{m}$ , and find excellent correspondence with the  $850\mu\text{m}$  detections of Geach et al. (2005). By analyzing the rest-frame UV, optical, and near/mid/far-infrared colors, and archival X-ray imaging, we show that these six systems exhibit signs of AGN activity and/or intense and dusty star formation; notably, they exhibit colors which bridge the star-forming LBG galaxies within the SSA22 structure and objects optically identified as QSOs. Through a stacking analysis see that the infrared faint LABs are markedly different than the infrared-luminous systems, and are consistent with blue star-forming galaxies, with no evidence of an AGN contribution. These results are in line with a model in which the LAB  $\text{Ly}\alpha$  luminosity is powered by large-scale superwinds, driven by star-formation in the smaller systems and a combination of AGN and extreme starbursts in the most massive. The presence of such a halo may be dictated by the evolutionary phase of the galaxy, such that the halo-less LBGs are older systems than the LABs. A scenario in which the LAB is the result of gravitational heating and the galactic activity is not driving the LAB luminosity cannot be ruled out, however.

Observations reported here were obtained at the MMT Observatory, a joint facility of the Smithsonian Institution and the University of Arizona.

*Facilities:* MMT, Spitzer, XMM, CXO

#### REFERENCES

- Alonso-Herrero, A. et al. 2006, *ApJ*, 640, 167  
 Basu-Zych, A. & Scharf, C. 2004, *ApJ*, 615, L85  
 Bauer, F.E., Alexander, D.M., Brandt, W.N., Schneider, D.P., Treister, e., Hornschemeier, A.E., & Garmire, G.P. 2004, *AJ*, 128, 2048  
 Beelen, A., et al. 2008, *A&A*, 485, 645  
 Blum, R.D. et al. 2006, *AJ*, 132, 2034  
 Bower, R.G., et al. 2004, *MNRAS*, 351, 63  
 Chapman, S. C., Lewis, G. F., Scott, D., Richards, E., Borys, C., Steidel, C. C., Adelberger, K. L., & Shapley, A.E. 2001, *ApJ*, 548, L17  
 Chapman, S. C., Smail, I., Windhorst, R., Muxlow, T., & Ivison, R.J. 2004, 611, 732  
 Chapman, S.C., Blain, A.W., Smail, I., Ivison, R.J. 2005, *ApJ*, 622, 772  
 Cirasuolo, M., McLure, R.J., Dunlop, J.S., Almaini, O., Foucaud, S., & Simpson, C. 2008, submitted to *MNRAS*, arXiv:0804.3471  
 Coil, A.L., Gerke, B.F., Newman, J.A., Ma, C.-P., Yan, R., Cooper, M.C., Davis, M., Faber, S., Guhathakurta, P., & Koo, D.C. 2006, *ApJ*, 638, 668  
 Colbert, J. W., Teplitz, H., Francis, P., Palunas, P., Williger, G. M., & Woodgate, B. 2006, *ApJ*, 637, L89  
 Coleman, G. D., Wu, C. -C., & Weedman, D. W. 1980, *ApJS*, 43, 393  
 Dey, A. et al. 2005, *ApJ*, 629, 654  
 Dey, A., et al. 2008, *ApJ*, in press.  
 Egami, E., et al. 2004, *ApJS*, 154, 130  
 Fabbiano, G. 1989, *ARA&A*, 27, 87  
 Fazio, G.G. et al. 2004, *ApJS*, 154, 10  
 Fine, S., et al. 2006, *MNRAS*, 373, 613  
 Francis, P.J., et al. 2001, *ApJ*, 554, 1001  
 Fynbo, J.U., Moller, P., & Warren, S.J. 1999, *MNRAS*, 305, 849  
 Geach, J. E. et al. 2005, *ApJ*, 649, 661  
 Geach, J.E., Smail, I., Chapman, S.C., Alexander, D.M., Blain, A.W., Stott, J.P., & Ivison, R.J. 2007, *ApJ*, 655, L9  
 Giavalisco, M., Steidel, C.C., Adelberger, K.L., Dickinson, M.E., Pettini, M., & Kellogg, M. 1998, *ApJ*, 503, 543  
 Gordon, K. D. et al. 2005, *PASP*, 117, 503  
 Granato, G. L., Silva, L., Iapi, A., Shankar, F., De Zotti, G., & Danese, L. 2006, *MNRAS*, 368, L72  
 Hayashino, T. et al. 2004, *AJ*, 128, 2073  
 Kaiser, N. 1984, *ApJ*, 284, L9  
 Kohno, K. et al. 2008, submitted  
 Keel, W.C., Cohen, S.H., Windhorst, R.A., Waddington, I. 1999, *AJ*, 118, 2547  
 Lacy, M. et al. 2004, *ApJS*, 154, 166  
 Lacy, M., Petric, A.O., Sajina, A., Canalizo, G., Storrie-Lombardi, L.J., Armus, L., Fadda, D., & Marleau, F.R. 2007, *AJ*, 133, 186  
 Le Fèvre, O. et al. 2005, *A&A*, 439, L877  
 Matsuda, Y., et al. 2004, *AJ*, 128, 569 (M04)  
 Matsuda, Y. et al. 2005, *ApJ*, 634, 125

- Matsuda, Y., Iono, D., Ohta, K., Yamada, T., Kawabe, R., Hayashino, T., Peck, A. B., & Petitpas, G. R. 2007, *ApJ*, 667, 667
- Palunas, P., Teplitz, H.I., Francis, P.J., Williger, G.M., Woodgate, B.E. 2004, *ApJ*, 602, 545
- Patton, D.R. et al. 2002, *ApJ*, 565, 208
- Pope, A. et al. 2006, *MNRAS*, 370, 1185
- Prescott, M.K.M., Kashikawa, N., Dey, A., Matsuda, Y. 2008, *ApJ*, 678, L77
- Reuland, M. et al. 2003, *ApJ*, 592, 755
- Rieke, G. et al. 2004, *ApJS*, 154, 25
- Rudnick, G., et al. 2007, *ApJ*, 650, 624
- Schuster, M. T., Marengo, M., & Patten, B. M. 2006, *SPIE*, 6270, 65
- Scott, J. E., Kriss, G. A., Brotherton, M., Green, R. F., Hutchings, J., Shull, J. M., & Zheng, W. 2004, *ApJ*, 615, 135
- Shang, Z. et al. 2005, *ApJ*, 619, 41
- Shapley, A.E., Steidel, C.C., Pettini, M., Adelberger, K.L. 2003, *ApJ*, 588, 65
- Smith, D.J.B., & Jarvis, M.J. 2007, *MNRAS*, 387, 49
- Steidel, C. C., Adelberger, K. L., Dickinson, M., Giavalisco, M., Pettini, M., & Kellogg, M. 1998, *ApJ*, 492, 428
- Steidel, C.C., Adelberger, K.L., Shapley, A.E., Pettini, M., Dickinson, M., Giavalisco, M. 2002, *ApJ*, 523, 170
- Steidel C. C., M., Adelberger, K. L., Shapley, A. E., Pettini, M., Dickinson, M., & Giavalisco, M. 2003, *ApJ*, 592, 728
- Stern, D. et al. 2005, *ApJ*, 631, 163
- Webb, T.M.A., Eales, S.A., Lilly, S.J., Clements, D.L., Dunne, L., Gear, W.K., Ivison, R.J., Flores, H., & Yun, M. 2003, *ApJ*, 587, 41
- Werner, M. W. et al. *ApJS*, 154, 1
- Yun, S. et al. 2008, *MNRAS*, in press